Proceedings of the ASME 2013 International Design Engineering Technical Conferences & Computers and Information in Engineering Conference
IDETC/CIE 2013
August 4-7, 2013, Portland, OR, USA

DETC/CIE2013-13015

PERFORMANCE ANALYSIS AND EXPERIMENTAL VALIDATION OF THE DIRECT STRAIN IMAGING METHOD

Athanasios Iliopoulos
Computational Materials Science Center
George Mason University, Fairfax VA 22030, USA
resident at Center of Computational Material Science
Naval Research Laboratory
Washington DC 20375, USA

John G. Michopoulos
Computational Multiphysics Systems Lab.
Center of Computational Material Science
Naval Research Laboratory
Washington DC, USA

John C. Hermanson
Wood Based Materials & Structures
Forest Products Laboratory
USDA Forest Service
Madison, WI, USA

1 Abstract

Direct Strain Imaging accomplishes full field measurement of the strain tensor on the surface of a deforming body, by utilizing arbitrarily oriented engineering strain measurements originating from digital imaging. In this paper an evaluation of the method's performance with respect to its operating parameter space is presented along with a preliminary validation based on actual experiments on composite material specimens under tension. It has been shown that the method exhibits excellent accuracy characteristics and outperforms methods based on displacement differentiation.

2 Introduction

Classical methods for experimental full field measurements [1–15] rely on accomplishing strain measurements by differentiation of the full field of displacement. On the contrary, the recently introduced Direct Strain Imaging (DSI) method performs the identification of the strains at any point on the region of interest directly from directional engineering strain components. This shift in the analytical basis of full field measurements implies a shift in both the semantic and accuracy contexts of the experimental method.

Although the initial goal of the computational framework behind DSI for the purpose of full field measurements was to enable the separation of the measurement from the continuity assumptions of the underlying medium [16], it was made evident at the same time that the new approach was also more accurate than traditional approaches. Specifically, it was shown that DSI outperforms methods based on Mesh Free approximations by a factor ranging from 1.2 to 3.6 for typical experimental conditions, both at regions close to irregularities and for the entire field [16, 17]. This observation motivated the investigation described in the present paper for the quantification of the performance of DSI mainly in terms of its accuracy characteristics as a function of user-controlled parameters.

Consequently, this paper aims at both presenting an analysis of the accuracy of DSI as it relates to the parameters that affect its performance, and at presenting its validation based on comparing its measurements with strain gauge data collected from actual experiments. The performed parametric study is based on

This material is declared a work of the U.S. Government and is not subject to copyright protection in the United States.
Approved for public release; distribution is unlimited.

the basic DSI factors such as the positional accuracy of the measuring nodes, the distance between those nodes and the extent of the domain of influence of the mesh-free representation of the strain tensor. This study is performed on the non uniform strain field resulting from the deformation of an orthotropic plate with a circular hole loaded at infinity. Our choice of synthetic experiment geometry is more realistic and more demanding when compared with synthetic experiments performed for verification of other methods [18], where the corresponding strain fields are expressed by low order polynomials applied on simply connected domains. The experimental validation is performed on doubly notched composite specimen tension experiments using strain gauge data.

The paper begins with a brief introduction to the DSI method for full field measurements along with its algebraic formulation. It then continues with the description of the synthetic experiments performed and the definition of the parametric space. The results of the parametric analysis are presented next, together with a discussion on the evaluation of the DSI performance. The last section presents a DSI validation effort based on actual experiments conducted with NRL's 6-DoF multiaxial loader [19–21] where strains derived from application of DSI are compared to those originating from strain gauge based measurements. The paper concludes with the most important observations and suggestions for future research.

3 Brief description of the DSI method

The typical experimental procedure for measuring the full field of deformation quantities according to the DSI method can be outlined as follows. A specimen is marked with an appropriate visible pattern that consists of a distribution (random or regular) of dots distinguishable from the background. If the experiment is to take into consideration out of plane motion, two or more cameras are used so that the deformation is stereoscopically reconstructed. The projective characteristics of the cameras are identified through an appropriate calibration procedure [8, 22]. The specimen is placed in the mechanical testing machine and one image per camera is captured in the undeformed configuration prior to the initiation of the loading sequence. While the experiment is taking place, successive images of the deforming specimen are captured. The images are processed and for each frame, the coordinates of appropriate points (nodes) are calculated. Those nodes may be for example geometric centroids of dots (for the case of grid methods), appropriate boundaries of geometric entities, correlated sub regions, etc. A set of nodes in the vicinity of each point $\mathbf{w} = \{x_w, y_w\}^T$ in the full field representation are considered and their in-between distances l_{ij} and l'_{ij} are calculated in the undeformed (Fig. 1(a)) and deformed (Fig. 1(b)) configurations respectively. For each of those node pairs the engineering strain is calculated by $e_{ij} = \left(l'_{ij} - l_{ij}\right)/l_{ij}, i = 1 \ldots n-1, j = 2 \ldots n, i < j$. The strain tensor components at the point $\mathbf{w}$ are calculated using the DSI approximation scheme as described in the paragraphs that follow.

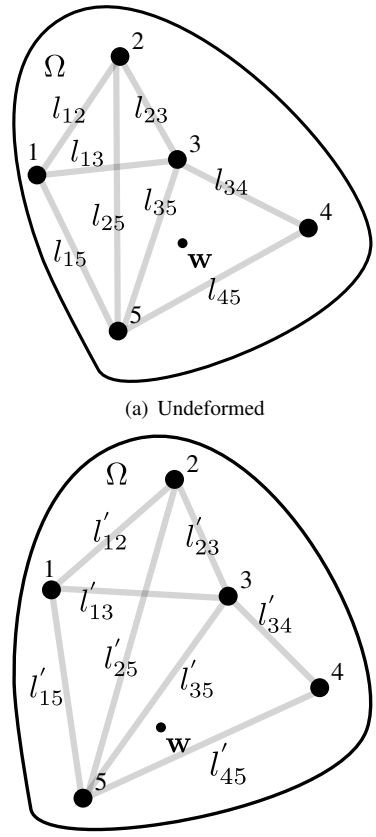

(a) Undeformed

(b) Deformed

FIGURE 1: DEFORMATION CONFIGURATIONS AND DISTANCES OF SELECTED NODE PAIRS.

Noise introduced in the digital imaging setup by various sources is the most dominant source of error and plagues all full field measurement methods. Because of the very good noise mitigating attributes of the DSI method, it has been shown that the effects of this noise is greatly reduced in comparison with other methods, even when compared to the MRG method [16].

The engineering strain between pairs of adjacent centroids of dots (nodes) along the directions defined by them, is the digitally determined data input for the DSI analysis. A domain Ω in the undeformed configuration is shown in Fig. 1(a), populated with a number of such nodes. The same domain in the deformed configuration is shown in 1(b). For a set of n nodes in the vicinity of an interest point described by a position vector $\mathbf{w} = \{x_w, y_w\}^T$, it is possible to form a number of engineering strain quantities $e_{ij} = \left(l'_{ij} - l_{ij}\right)/l_{ij}, i = 1 \ldots n-1, j = 2 \ldots n, i < j$ [23] in terms of the distances l_{ij}, l'_{ij} in the initial and deformed configurations

This material is declared a work of the U.S. Government and is not subject to copyright protection in the United States.
Approved for public release; distribution is unlimited.

respectively. Each of those quantities can be considered as the mean of the strain component in the direction of the line connecting the two nodes over the respective line segment. Given those engineering strains and the coordinates of the nodes, DSI can be used to calculate the strain tensor at any point $\mathbf{w}$ in the domain. It is important to note that similarly with traditional meshless methods [24–26] the vicinity of a point of interest $\mathbf{w} = \{x_w, y_w\}^T$ is bound by an appropriate Domain Of Support (DOS), and in this work we will consider the DOS to be circular.

In the following paragraphs, only the essential formulas for the DSI evaluation will be presented. A detailed description of the solution to this problem can be found in [16].

According to [16], the DSI strains are calculated by,

$$\left.\begin{aligned} \varepsilon_{xx}^h(\mathbf{w}) &= \mathbf{\Phi}_{xx}(\mathbf{w})\,\mathbf{e_w} \\ \varepsilon_{yy}^h(\mathbf{w}) &= \mathbf{\Phi}_{yy}(\mathbf{w})\,\mathbf{e_w} \\ \varepsilon_{xy}^h(\mathbf{w}) &= \mathbf{\Phi}_{xy}(\mathbf{w})\,\mathbf{e_w} \end{aligned}\right\}, \tag{1}$$

where,

$$\mathbf{e_w} = \left\{e_{21}, e_{31}, e_{32}, e_{41}, e_{42,} \ldots, e_{ij}, \ldots, e_{n(n-1)}\right\}^T, \tag{2}$$

is a vector that collects all the measured engineering strains in the vicinity of $\mathbf{w}$ for all pairs of points i, j with position vectors $\mathbf{x}_i = \{x_i, y_i\}^T$ and $\mathbf{x}_j = \left\{x_j, y_j\right\}^T$. Additionally,

$$\mathbf{\Phi}_\alpha(\mathbf{w}) = \mathbf{p}^T(\mathbf{w})\,\mathbf{M}_\alpha(\mathbf{w}), \tag{3}$$

are shape functions of the strain components for the point $\mathbf{w}$ for $\alpha = xx, yy, xy$. $\mathbf{p}(\mathbf{x})$ is a vector of basis functions that can be chosen to consist of m monomials of the lowest orders to ensure minimum completeness. A polynomial basis of order $M < m$ has the general form,

$$\mathbf{p}(\mathbf{x}) = \mathbf{p}(x,y) = \{1, x, y, xy, x^2, y^2, \ldots, x^M, y^M\}^T. \tag{4}$$

Such a polynomial basis can be constructed by concatenation of the complete order terms using the Pascal triangle of monomials [24, 26]. The terms $\mathbf{M}_\alpha$ in Eq. (3) are identified by a proper partiationing of the matrix,

$$\mathbf{M}(\mathbf{w}) = \begin{bmatrix} \mathbf{M}_{xx}(\mathbf{w}) \\ \mathbf{M}_{yy}(\mathbf{w}) \\ \mathbf{M}_{xy}(\mathbf{w}) \end{bmatrix}. \tag{5}$$

that can be calculated by solving,

$$\mathbf{Q}(\mathbf{w})\,\mathbf{M}(\mathbf{w}) = \mathbf{B}(\mathbf{w}) \tag{6}$$

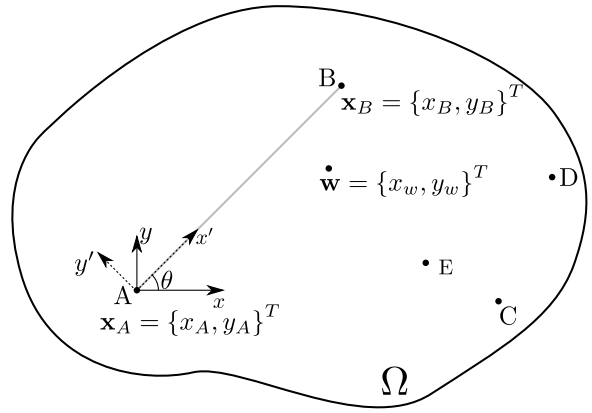

FIGURE 2: COORDINATE DEFINITIONS FOR A PAIR OF POINTS A, B IN THE VICINITY OF $\mathbf{w}$ RELATIVE TO THE LOCAL COORDINATE SYSTEM AT POINT A.

$\mathbf{B}$ is a matrix that has the form,

$$\left.\begin{aligned} \mathbf{B}(\mathbf{w}) &= \left[\mathbf{b}_{21}, \mathbf{b}_{31}, \mathbf{b}_{32}, \mathbf{b}_{41}, \mathbf{b}_{42}, \ldots, \mathbf{b}_{n(n-1)}\right] \\ \mathbf{b}_{ij}(\mathbf{w}) &= W\left(\mathbf{w} - \frac{\mathbf{x}_i + \mathbf{x}_j}{2}\right)\mathbf{q}(\mathbf{x}_i, \mathbf{x}_j) \end{aligned}\right\}, \tag{7}$$

and $\mathbf{Q}(\mathbf{w})$ is defined by,

$$\mathbf{Q}(\mathbf{w}) = \sum_{i=1, j=2, i<j}^{n-1, n} W\left(\mathbf{w} - \frac{\mathbf{x}_i + \mathbf{x}_j}{2}\right)\mathbf{q}(\mathbf{x}_i, \mathbf{x}_j)\,\mathbf{q}^T(\mathbf{x}_i, \mathbf{x}_j), \tag{8}$$

where $W(\mathbf{w} - (\mathbf{x}_i + \mathbf{x}_j)/2) = W_{ij} \geq 0$ is a weight function that decreases with distance as introduced by [24, 26]. A common weight function is the cubic spline weight function given by,

$$W(\mathbf{d}) \equiv W(\hat{d}) = \begin{cases} \frac{2}{3} - 4\hat{d}^2 + 4\hat{d}^3 & , \hat{d} \leq \frac{1}{2} \\ \frac{4}{3} - 4\hat{d} + 4\hat{d}^2 - \frac{4}{3}\hat{d}^3 & , \frac{1}{2} < \hat{d} \leq 1 \\ 0 & , \hat{d} > 1 \end{cases} \tag{9}$$

with $\hat{d} = \frac{|\mathbf{d}|}{d_w}$, the normalized distance, and d_w the smoothing length that is usually equal to the extend of the domain of support.

The terms $\mathbf{q}(\mathbf{x}_i, \mathbf{x}_j)$ in Eqn. (8) are given by,

$$\left.\begin{aligned} \mathbf{q}_{xx}^T(\mathbf{x}_i, \mathbf{x}_j) &= \mathbf{r}^T(\mathbf{x}_i, \mathbf{x}_j)\cos^2\theta \\ \mathbf{q}_{yy}^T(\mathbf{x}_i, \mathbf{x}_j) &= \mathbf{r}^T(\mathbf{x}_i, \mathbf{x}_j)\sin^2\theta \\ \mathbf{q}_{xy}^T(\mathbf{x}_i, \mathbf{x}_j) &= \mathbf{r}^T(\mathbf{x}_i, \mathbf{x}_j)\sin 2\theta \end{aligned}\right\}. \tag{10}$$

This material is declared a work of the U.S. Government and is not subject to copyright protection in the United States.
Approved for public release; distribution is unlimited.

with $\mathbf{x}_i$, $\mathbf{x}_j$ the vector representations of each pair of points i, j and θ the angle relative to the global system of reference of the line segment that connects those points as shown in Fig. 2 for two points A and B.

The terms $\mathbf{r}^T(\mathbf{x}_i, \mathbf{x}_j)$ are vector integrals [16] and can be derived from the terms of Table 1. If a full order polynomial is chosen, the integral basis vector can be constructed by concatenation of the respective terms. For example if a 6 term basis vector is chosen to be $\mathbf{p}(\mathbf{x}) = \mathbf{p}(x,y) = \{1, x, y, xy, x^2, y^2\}^T$, the integral basis vector will be,

$$\mathbf{r}^T(\mathbf{x}_A, \mathbf{x}_B) = \int_0^1 \mathbf{p}^T(\mathbf{s}(\mathbf{x}_A, \mathbf{x}_B; \lambda))\, d\lambda = \left\{1, \frac{1}{2}(x_A + x_B), \frac{1}{2}(y_A + y_B), \frac{1}{6}(x_A(2y_A + y_B) + x_B(y_A + 2y_B)), \frac{1}{3}(x_A^2 + x_A x_B + x_B^2), \frac{1}{3}(y_A^2 + y_A y_B + y_B^2)\right\}. \tag{11}$$

with $\mathbf{s}(\mathbf{x}_A, \mathbf{x}_B; \lambda), \lambda \in [0,1]$, the parametric representation of the line segment AB. In any case, the choice of an appropriate polynomial basis will yield an integral vector basis $\mathbf{r}^T(\mathbf{x}_A, \mathbf{x}_B)$.

4 Synthetic experiment design

In order to obtain metric characteristics of the response of DSI relative to the parameters controlling it, various parametric studies were designed and performed on synthetic experiments. All the synthetic experiments are considered to be mapped on a digital imaging grid of 1600×1600 pixels. The performance analysis of DSI was performed on an analytically known deformation field of an orthotropic plate with an open hole. The analytic representation of that problem is presented in the next subsection.

The parameters of interest for the parametric study include the mean node distance (considering a uniform distribution), the positional accuracy as a property of the imaging setup and the domain of support. In previous studies [13], the performance was investigated also over imaging characteristics (namely the bit depth and the gray-scale intensity), that in the current study are both represented by the positional accuracy. The results of [13] suggest that for common imaging setups the positional accuracy is at the level of 1×10^{-2} pixels but it can range approximately between 1×10^{-1} and 1×10^{-4} pixels. The final values chosen for the positional accuracy of each node where $1/16, 1/32, 1/64, 1/128, 1/256, 1/512, 1/1024, 1/8192, 0$ pixels and they were applied through a Gaussian noise function on the computed displacement provided by the analytical solution. A value of zero represents the absence of noise and is used as a basis for studying the numerical characteristics of DSI.

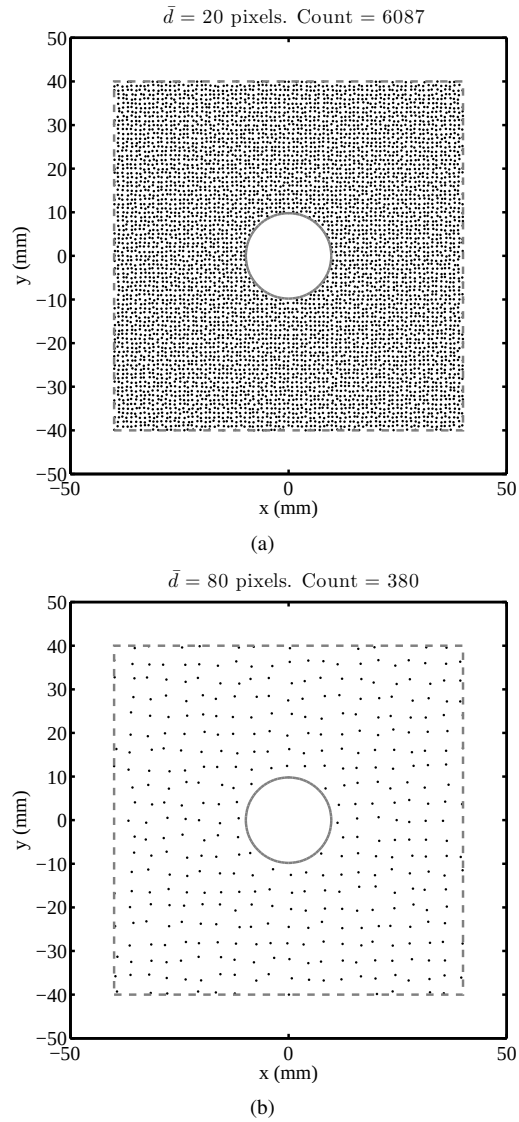

FIGURE 3: SAMPLE SYNTHETIC EXPERIMENT NODE DISTRIBUTIONS FOR (a) MEAN DOT DISTANCE OF 20 PIXELS, (b) MEAN DOT DISTANCE OF 80 PIXELS. THE DOMAIN IS ASSUMED TO SPAN 1600×1600 PIXELS.

An important characteristic that can be chosen by the user of the DSI method is that of the mean distance between the dots marked on the specimen. A denser distribution of dots results in higher spatial resolution of the representation but choosing a denser over a coarser distribution is not always the right choice. The reason for that is that in order to accommodate more dots in a certain area, those dots have to be smaller than the dots on an area marked with a coarser grid. The smaller dots result in lower positional accuracy as demonstrated in [13]. Hence depending on the expected deformation field some compromises have to be

This material is declared a work of the U.S. Government and is not subject to copyright protection in the United States.
Approved for public release; distribution is unlimited.

TABLE 1: INTEGRAL BASIS MONOMIALS

Complete Order	No. of Terms	Additional Terms
Constant	1	1
Linear	3	$\left\{\frac{1}{2}\left(x_A+x_B\right),\frac{1}{2}\left(y_A+y_B\right)\right\}$
Bi-linear	4	$\frac{1}{6}\left(x_A\left(2y_A+y_B\right)+x_B\left(y_A+2y_B\right)\right)$
Quadratic	6	$\left\{\frac{1}{3}\left(x_Ax_B+x_A^2+x_B^2\right),\frac{1}{3}\left(y_Ay_B+y_A^2+y_B^2\right)\right\}$
Quadratic	8	$\left\{\frac{1}{12}\left(x_A^2\left(3y_A+y_B\right)+2x_Ax_B\left(y_A+y_B\right)+x_B^2\left(y_A+3y_B\right)\right),\right.$ $\left.\frac{1}{12}\left(y_A^2\left(3x_A+x_B\right)+2y_Ay_B\left(x_A+x_B\right)+y_B^2\left(x_A+3x_B\right)\right)\right\}$
Cubic	10	$\left\{\frac{1}{4}\left(x_A+x_B\right)\left(x_A^2+x_B^2\right),\frac{1}{4}\left(y_A+y_B\right)\left(y_A^2+y_B^2\right)\right\}$
Quartic	15	$\left\{\frac{1}{20}\left(x_A^3\left(4y_A+y_B\right)+x_A^2x_B\left(3y_A+2y_B\right)+x_Ax_B^2\left(2y_A+3y_B\right)+\right.\right.$ $\left.+x_B^3\left(y_A+4y_B\right)\right),$ $\frac{1}{30}\left(x_A^2\left(3y_Ay_B+6y_A^2+y_B^2\right)+x_Ax_B\left(4y_Ay_B+3y_A^2+3y_B^2\right)+\right.$ $\left.+x_B^2\left(3y_Ay_B+y_A^2+6y_B^2\right)\right),$ $\frac{1}{20}\left(y_A^3\left(4x_A+x_B\right)+y_A^2y_B\left(3x_A+2x_B\right)+y_Ay_B^2\left(2x_A+3x_B\right)+\right.$ $\left.+y_B^3\left(x_A+4x_B\right)\right),$ $\frac{1}{5}\left(x_A^3x_B+x_A^2x_B^2+x_Ax_B^3+x_A^4+x_B^4\right),$ $\left.\frac{1}{5}\left(y_A^3y_B+y_A^2y_B^2+y_Ay_B^3+y_A^4+y_B^4\right)\right\}$

made by the user in order to obtain desirable full field distribution characteristics. To study the effects of the dot distribution, the synthetic experiment data included varying the mean dot distribution from 10 to 80 pixels with a step of 10. Sample dot distributions are presented in Fig. 3

The last parameter that was studied was that of the DOS. Higher DOS generally results in higher precision but less accuracy. According to [26] a good value for Mesh-Free approximations is around 2.4×mean dot distance, but of course in this case it refers to fields without noise. In the current analysis the effect of DOS was studied by varying it with respect to each of the mean dot distance parametric cases for values $1.6, 1.8, 2.0, 2.2, 2.4, 2.6, 3.0, 3.5, 4.0, 4.5, 5$ and 7.5.

For each synthetic experiment the following steps were followed:

1. A random distribution of dots was generated based on a mean dot distance (Fig. 3).
2. Given the analytic solution of a predefined problem, material properties and bounary conditions, the displacement on each of the dots (assumed to be nodes) was calculated.
3. The displaced nodes were perturbed by a certain amount based on a random function sampled from a Gaussian distribution for each chosen noise value
4. The DSI procedure was applied on the un-deformed and deformed nodes and the error metrics where calculated for each value of the DOS.

The error metric used in this study was the mean absolute strain difference between the DSI solution and the analytical solution,

$$e_\alpha = \frac{\sum_{i=1}^{N}\left|{}^i\varepsilon_\alpha^a - {}^i\varepsilon_\alpha^{dsi}\right|}{N} \tag{12}$$

where N is the number of evaluation points, $\alpha = xx, yy, xy$ is the strain component of interest, ${}^i\varepsilon_\alpha^a$ is the analytic solution at the evaluation point i and ${}^i\varepsilon_\alpha^{dsi}$ is the DSI result at the evaluation point i. The error metric calculation was performed on two sets of points, (a) the entire domain and (b) points on a circular domain around the hole. Those two sets are shown in Fig. 4.

This material is declared a work of the U.S. Government and is not subject to copyright protection in the United States.
Approved for public release; distribution is unlimited.

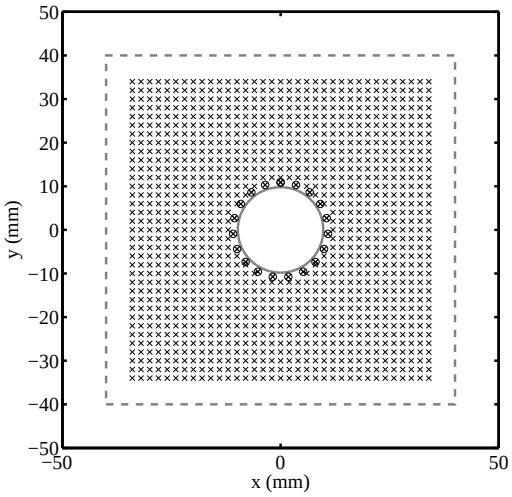

FIGURE 4: THE EVALUATION POINTS FOR THE ERROR METRIC CALCULATION. THE POINTS MARKED WITH AN $\times$ REPRESENT THE CALCULATION ON THE FULL DOMAIN, WHILE THE POINTS THAT ARE ADDITIONALLY MARKED WITH AN O REPRESENT THE ERROR METRIC CALCULATION CLOSE TO THE BOUNDARY.

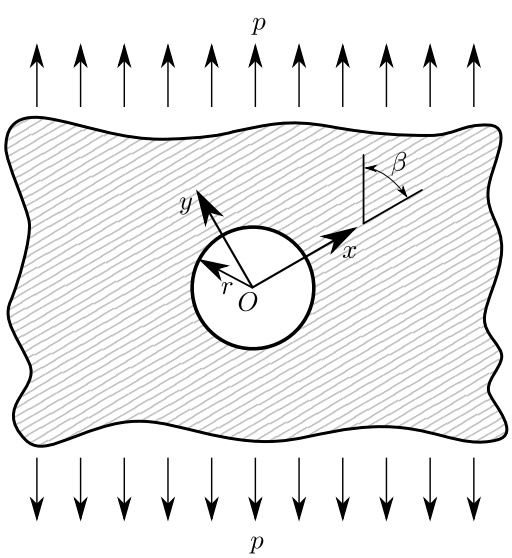

FIGURE 5: ORTHOTROPIC PLATE WITH AN OPEN HOLE AND LOAD AT INFINITY.

4.1 Orthotropic plate with open hole

Although the analytic representation of the following problem is also presented elsewhere [16], it is also included here for completeness. We consider an infinitely large orthotropic elastic plate that contains a circular hole of radius r that is subjected to a stress state at infinity equal to p. The applied load forms an angle β with the major orthotropic axis as shown in Fig. 5. This angle essentially controls the degree of anisotropy introduced in the strain-stress fields and varying it amounts for rotating the major orthotropic axis relative to the loading direction (i.e. dual description of the angle). Strain at any point on the plane is expressed by the elastic constitutive equations [27] in terms of the respective stress components as follows,

$$\left.\begin{aligned} \varepsilon_{xx} &= a_{11}\sigma_{xx} + a_{12}\sigma_{yy} + a_{16}\tau_{xy} \\ \varepsilon_{yy} &= a_{12}\sigma_{xx} + a_{22}\sigma_{yy} + a_{26}\tau_{xy} \\ \gamma_{xy} &= a_{16}\sigma_{xx} + a_{26}\sigma_{yy} + a_{66}\tau_{xy} \end{aligned}\right\}. \tag{13}$$

In the mathematical theory of elasticity it has been shown [27] that the composition of the force equilibrium differential equations along with the constitutive Eqns. (13) for the general case of multiply connected plane problems, can be reduced to a set of algebraic equations in terms of holomorphic functions expressed in the complex plane. In fact, the general solution to this problem for an elliptic hole is known [28] and is implemented here for an ellipse of minor to major axes aspect ratio of unity, in order to reflect the problem when the hole is circular. Additional modifications have been introduced [29] to account for rotations of the medium at infinity.

The stresses are calculated by the equations [28],

$$\left.\begin{aligned} \sigma_{xx} &= \sigma_{xx}^{\infty} + 2\mathrm{Re}\left[{s_1}^2\frac{\partial\phi_0(z_1)}{\partial z_1} + {s_2}^2\frac{\partial\psi_0(z_2)}{\partial z_2}\right] \\ \sigma_{yy} &= \sigma_{yy}^{\infty} + 2\mathrm{Re}\left[\frac{\partial\phi_0(z_1)}{\partial z_1} + \frac{\partial\psi_0(z_2)}{\partial z_2}\right] \\ \tau_{xy} &= \tau_{xy}^{\infty} - 2\mathrm{Re}\left[s_1\frac{\partial\phi_0(z_1)}{\partial z_1} + s_2\frac{\partial\psi_0(z_2)}{\partial z_2}\right] \end{aligned}\right\}, \tag{14}$$

where, s_1, s_2 are the roots of,

$$a_{11}s^4 - 2a_{16}s^3 + (2a_{12} + a_{66})s^2 - 2a_{26}s + a_{22} = 0. \tag{15}$$

Equation (15) has no real roots and are therefore always of the form [27],

$$s_{1,3} = a_1 \pm b_1 i,\ s_{2,4} = a_2 \pm b_2 i,\ b_1 > 0, b_2 > 0. \tag{16}$$

The stress state at infinity is given by,

$$\sigma_{xx}^{\infty} = p\cos^2\beta,\ \sigma_{yy}^{\infty} = p\sin^2\beta,\ \tau_{xy}^{\infty} = p\cos\beta\sin\beta, \tag{17}$$

while the holomorphic functions are,

$$\left.\begin{aligned} \varphi_0(z_1) &= -\frac{ir\left[\sigma_x^{\infty} + is_2\sigma_y^{\infty} + (s_2+i)\tau_{xy}^{\infty}\right]}{2(s_1-s_2)}\zeta_1(z_1) \\ \psi_0(z_2) &= -\frac{ir\left[\sigma_x^{\infty} + is_1\sigma_y^{\infty} + (s_1+i)\tau_{xy}^{\infty}\right]}{2(s_1-s_2)}\zeta_2(z_2) \end{aligned}\right\}, \tag{18}$$

This material is declared a work of the U.S. Government and is not subject to copyright protection in the United States.
Approved for public release; distribution is unlimited.

where:

$$\left.\begin{aligned}\zeta_1(z_1) &= \frac{z_1 \pm \sqrt{z_1^2 - r^2\left(1+s_1^2\right)}}{r(1+is_1)} \\ \zeta_2(z_2) &= \frac{z_2 \pm \sqrt{z_2^2 - r^2\left(1+s_2^2\right)}}{r(1+is_2)}\end{aligned}\right\}. \tag{19}$$

The sign ambiguity in Eqns. (19) is removed by requiring $|\zeta_1| \leq 1$ and $|\zeta_2| \leq 1$. The complex variables are defined in terms of the real position coordinates according to: $z_1 = x + s_1 y$ and $z_2 = x + s_2 y$. Finally, the displacement field components at Ox and Oy directions are given by [29],

$$\left.\begin{aligned}u &= 2\mathrm{Re}\left[p_1\varphi_0(z_1) + p_2\psi_0(z_2)\right] + x\varepsilon_{xx}^{\infty} + y\varepsilon_{xy}^{\infty} \\ v &= 2\mathrm{Re}\left[q_1\varphi_0(z_1) + q_2\psi_0(z_2)\right] + y\varepsilon_{yy}^{\infty} + x\varepsilon_{xy}^{\infty}\end{aligned}\right\}, \tag{20}$$

with,

$$\left.\begin{aligned}p_1 &= a_{11}{s_1}^2 + a_{12} - a_{16}s_1 \\ p_2 &= a_{11}{s_2}^2 + a_{12} - a_{16}s_2 \\ q_1 &= \frac{a_{12}{s_1}^2 + a_{22} - a_{26}s_1}{s_1} \\ q_2 &= \frac{a_{12}{s_2}^2 + a_{22} - a_{26}s_2}{s_2}\end{aligned}\right\}. \tag{21}$$

4.2 Numerical Experiments

The synthetic experiments were performed by implementing the DSI algorithmics in Matlab [30] on an a second generation Intel i7 four core processor (2960XM). The time required for the strain tensor evaluation per load increment as expressed by Eqns. (1) was found to be of order 10^{-3} seconds.

The radius of the hole was selected to be $a = 10^{-2}m$, the stress at infinity $\sigma_\infty = 2 \times 10^5 Pa$, the angle of the major orthotropic axis was $\beta = 45^o$ while the extend of the domain of interest (in both the x and y coordinates) was $8a$. The material properties were selected to be:

$$\begin{bmatrix} a_{11} & a_{12} & a_{16} \\ a_{12} & a_{22} & a_{26} \\ a_{16} & a_{22} & a_{66} \end{bmatrix} = \begin{bmatrix} 2.245 & -2.732 & 0.000 \\ -2.732 & 9.436 & 0.000 \\ 0.000 & 0.000 & 4.315 \end{bmatrix} \times 10^{-9} Pa^{-1} \tag{22}$$

The basis function for the DSI method was chosen to be of first order (a total of 3 terms).

In Fig. 6 the mean absolute error of the vertical strain component ε_{yy} is plotted versus the extent of the domain of support

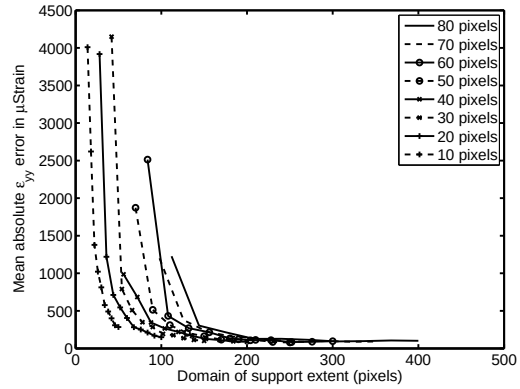

(a) Over the entire domain

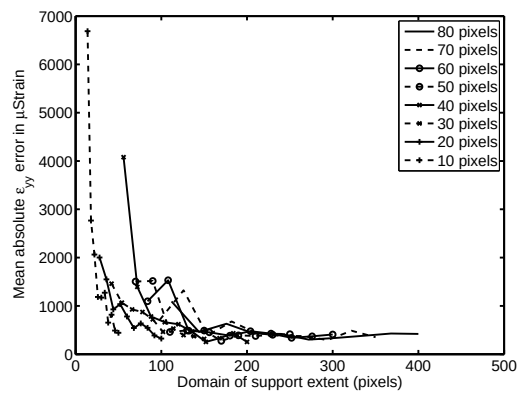

(b) On the boundary close to the circular hole

FIGURE 6: MEAN ABSOLUTE ERROR OF ε_{yy} FOR NOISE LEVEL $1/16$ PIXELS FOR DISTRIBUTIONS OF VARIOUS MEAN DOT DISTANCES IN PIXELS.

for both sets of evaluation points for noise levels of $1/16$ pixels. In both cases it is observed that larger domains of support result in reduced error, while the denser the grid, the more accurate the measurement. Note, this noise level is quite unrealistic, but it is used here to demonstrate the very good noise mitigating characteristics of the DSI method.

In Fig. 7 the same data is plotted for the case the noise level was $1/128$ pixels. This is a more realistic case and represents the noise levels one would expect from cameras with effective bit depth of about 8-10 bits. For most grid densities, an optimal value for the error is achieved for a DOS of about 100 pixels as shown in Fig. 7(a). The same observation can be made for the plot in Fig. 7(b). The mean absolute error is around 30 $\mu Strain$ for the point set of the entire field for most grid densities, while for the point set around the boundary is at the level of 100 $\mu Strain$

In the last of this set of plots (Fig. 8), the same error metrics are plotted for the case of lack of noise. In this case, very low error levels are achieved with values as low as 2 $\mu Strain$. Although

This material is declared a work of the U.S. Government and is not subject to copyright protection in the United States.
Approved for public release; distribution is unlimited.

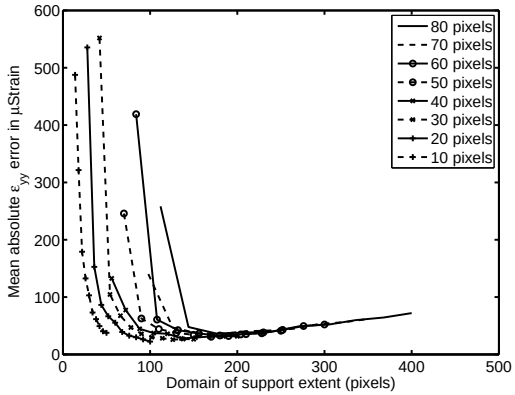

(a) Over the entire domain

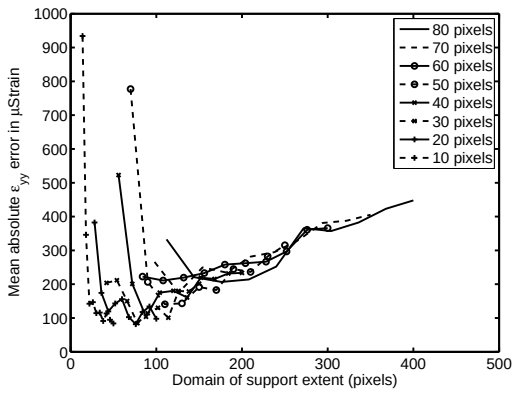

(b) On the boundary close to the circular hole

FIGURE 7: MEAN ABSOLUTE ERROR OF ε_{yy} FOR NOISE LEVEL $1/128$ PIXELS FOR DISTRIBUTIONS OF VARIOUS MEAN DOT DISTANCES IN PIXELS.

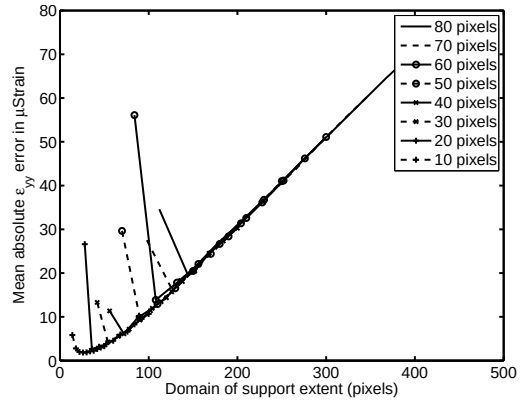

(a) Over the entire domain

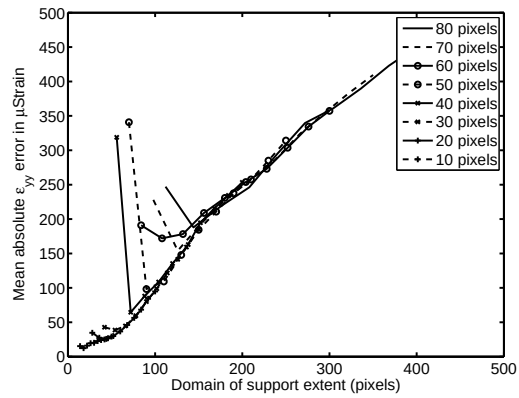

(b) On the boundary close to the circular hole

FIGURE 8: MEAN ABSOLUTE ERROR OF ε_{yy} FOR NOISE LEVEL OF 0 PIXELS FOR DISTRIBUTIONS OF VARIOUS MEAN DOT DISTANCES IN PIXELS.

cameras with noise that is lower than the error of numerical inaccuracies, do not currently exist, the plot can help us understand what is possible with the proposed tensor approximation scheme.

The mean absolute error with respect to the noise level for a mean dot distance of 40 pixels is presented in Fig. 9. This case represents a common choice of attributes that can be used with current digital imaging technology and reflects a practical situation. The expectation for the near future is that better digital imaging technology will enable the reduction of the mean dot distance by the virtue of lower noise for smaller dots [13]. For now, Fig. 9(a) suggests that it is currently possible to achieve a mean absolute error of around 20 $\mu Strain$, for the entire domain, while for the extreme case of the calculation on the boundary typical values for the mean absolute error metric are at the vicinity of 100 $\mu Strain$.

5 EXPERIMENTAL VALIDATION

The synthetic experiments provide the context for the verification (analytical validity) of the DSI method and also provide the basis for a direct approach for quantifying the actual error. The actual experimental validation is of equal importance as it demonstrates both the correctness and the efficiency of the DSI algorithmics as well as their computational implementation.

In order to experimentally validate the method, a number of tests were performed for a doubly notched specimen made out of AS4/3501-6 carbon epoxy composite. The width of the specimen was $50mm$, the free length (height between the grips) approximately $25mm$ and the thickness approximately $4.1mm$. On the right side of the specimen a strain gauge was attached (Fig. 10), while the left hand side was painted with a distribution of dots. The aim of the experimental test is to compare the vertical strain component as measured by the DSI and the strain gauge, within the uncertainties of the experimental setup.

The digital images captured had a size of 1600x1200 pixels

This material is declared a work of the U.S. Government and is not subject to copyright protection in the United States.
Approved for public release; distribution is unlimited.

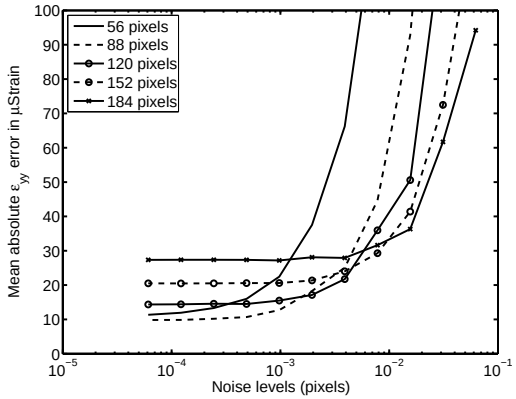

(a) Over the entire domain

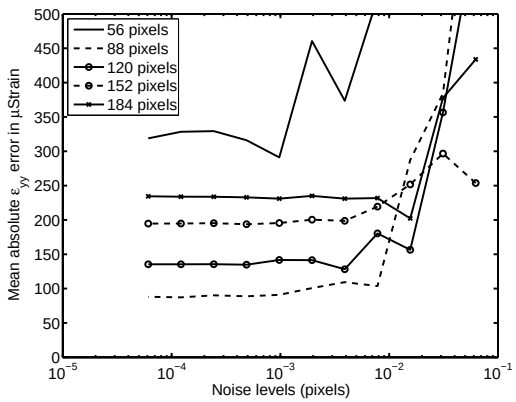

(b) On the boundary close to the circular hole

FIGURE 9: MEAN ABSOLUTE ERROR OF ε_{yy} FOR NOISE MEAN DOT DISTANCE OF 40 PIXELS.

with an effective bit depth of 10 bits (i.e. capable of representing about 2^{10} shades of gray). The total number of dots was 649 with an approximate mean distance of 35 pixels. The DSI domain of support was chosen to be 104 pixels, while the the basis function chosen was constructed by 3 terms. The single thread (non-parallelized) computational time required per frame, including image processing for centroid identification and DSI evaluation but not including hard disk read time or plotting the results, was found to be of the order of 0.2 seconds. This time is well within the limits required for a the real time application of the method.

The metric expressing the difference between the strain gauge and the DSI results was selected to be the mean average strain difference defined as:

$$\hat{\varepsilon} = \frac{\sum_{i=1}^{N} \left| \varepsilon_{sg} - \varepsilon_{dsi} \right|}{N} \tag{23}$$

where N is the number of frames of each of the experiments, ε_{sg}

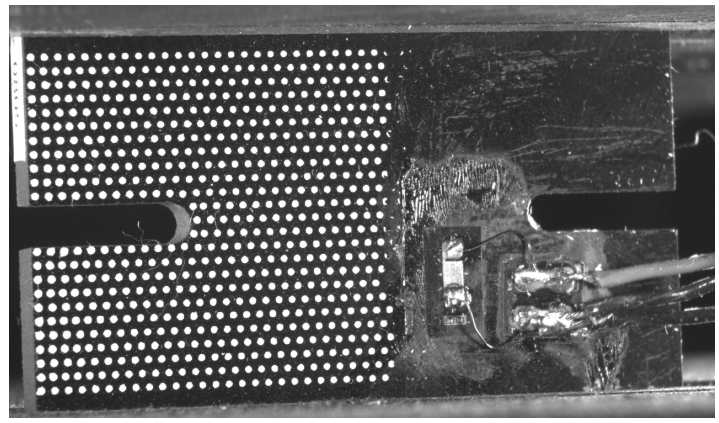

FIGURE 10: COMPOSITE SPECIMEN FOR EXPERIMENTAL VALIDATION OF THE DSI. THE LEFT SIDE IS PAINTED WITH A DISTRIBUTION OF DOTS FOR THE DSI CALCULATION, WHILE ON THE RIGHT SIDE A STRAIN GUAGE IS ATTACHED.

is the vertical strain (ε_{yy}) as measured by the strain gauge and ε_{dsi} is the vertical strain as measured by the DSI. Although this metric can give as an estimate of how well the strain gauge and the DSI data correlate, it would be unwise to use this quantity as an indication of the accuracy of DSI. An obvious reason for this argument lies on the fact that the data acquired by the strain gauge and DSI are not originating from the same position on the specimen. Material heterogeneity, specimen alignment, and testing machine aberrations, for example will induce strain variations that render absolute comparison fallible. Even if the sampling was done over the same points, the strain gauge positional and mounting uncertainty will still weaken the validation character of this effort.

Three tension tests were conducted using the NRL66.3 6 DoF robotic loader [20, 21, 31] and the results are shown in Fig. 11. The average of the absolute strain difference was 53.7 $\mu Strain$, 46.7 $\mu Strain$, 58.5 $\mu Strain$ for the first, second and third experiments respectively. Having in mind the experimental uncertainties and the mean error expected based on the synthetic experiment study of the previous section (which is at the level of $20-30$ $\mu Strain$), it can be concluded that the strain gauge and the DSI result are very close to each other.

6 CONCLUSIONS

In this paper a parametric analysis study was conducted and utilized synthetic experiments in order to evaluate the performance of the Direct Strain Imaging (DSI) method for a variety of user chosen parameters. Those included the mean dot distance painted on the surface of a specimen, the noise of the digital imaging setup and the extent of the domain of support of the

This material is declared a work of the U.S. Government and is not subject to copyright protection in the United States.
Approved for public release; distribution is unlimited.

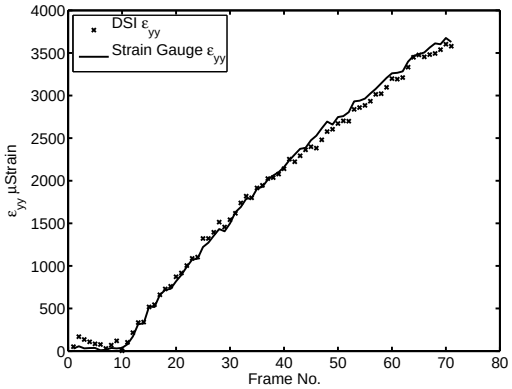

(a) Experiment 1: Mean absolute difference 53.7 $\mu Strain$

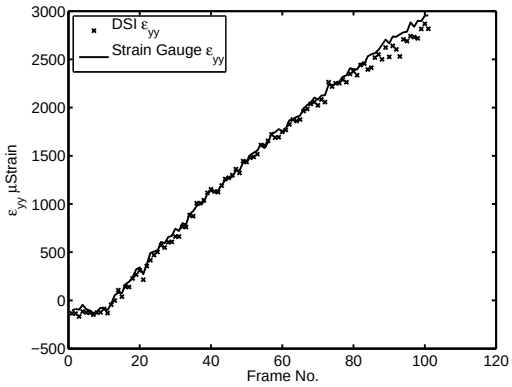

(b) Experiment 2: Mean absolute difference 46.7 $\mu Strain$

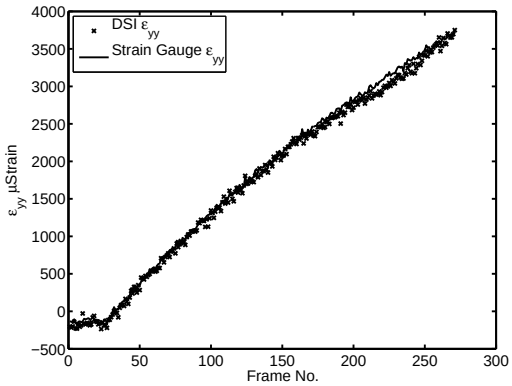

(c) Experiment 3: Mean absolute difference 58.5 $\mu Strain$

FIGURE 11: DSI VERTICAL STRAIN AND STRAIN GAUGE DATA FROM THE TENSION EXPERIMENTS.

DSI method.

It was demonstrated that for the current state of digital imaging technology, DSI is capable of providing full field representation of experimental data with a mean absolute error at the range of $20-30$ $\mu Strain$. This result makes DSI more accurate than the Meshless Random Grid method [13]. In the near future, as digital imaging technology evolves even more, the error of DSI can be reduced even further to levels even below 10 $\mu Strain$.

In addition, validation performance evaluation was conducted through the comparison of strain-gauge based experimental data and DSI based data. While absolute number comparison is tenuous for the reasons noted above, DSI matches exceptionally well with the strain gauge time history measurements.

DSI has shown excellent stability characteristics [16] and as presented in this paper is capable of very high accuracy measurements. Preliminary quantification of the computational cost indicate that the method has an excellent potential for real time applications. Finally, both the observed computational efficiency and the high accuracy of the DSI method also justify the future development of a time-filtering algorithm that will make it possible to reduce the error even further.

ACKNOWLEDGMENT

The authors acknowledge the support by the 6.1 core funding of the Naval Research Laboratory.

REFERENCES

[1] Sevenhuijsen, J., 1981. "Two simple methods for deformation demonstration and measurement". *Strain,* ***17***(1), pp. 20–24.

[2] Andersen, K., and Helsch, R., 1988. "Calculation of grating co-ordinates using correlation filter techniques". *Optik,* ***80***, pp. 76–79.

[3] Bruck, H., McNeill, S., Sutton, M., and Peters, W., 1989. "Digital image correlation using Newton-Raphson method of partial differential correction". *Experimental Mechanics,* ***29***, pp. 261–267. 10.1007/BF02321405.

[4] Sirkis, J., and Lim, T., 1991. "Displacement and strain measurement with automated grid methods". *Experimental Mechanics,* ***31***, pp. 382–388. 10.1007/BF02325997.

[5] Andrianopoulos, N. P., and Iliopoulos, A. P., 2005. *Strain measurements by a hybrid experimental-numerical method using a mesh-free field function, Honorary Volume for Professor P. S. Theocaris*. Armenian Academy of Sciences, pp. 31–41.

[6] Andrianopoulos, N. P., 2006. "Full-Field displacement measurement of a speckle grid by using a Mesh-Free deformation function". *Strain,* ***42***(4), pp. 265–271.

[7] Andrianopoulos, N. P., and Iliopoulos, A. P., 2006. "Displacements measurement in irregularly bounded plates using mesh free methods". In Proc. 16th European Conference of Fracture, Alexandroupolis, Greece, July 3–7.

[8] Iliopoulos, A. P., 2007. "Digital image processing on experimental mechanics and applications on metallic sheets". PhD thesis, National Technical University of Athens.

[9] Iliopoulos, A. P., and Andrianopoulos, N. P., 2008. "An

This material is declared a work of the U.S. Government and is not subject to copyright protection in the United States.
Approved for public release; distribution is unlimited.

approach to analyse errors introduced in the random grid strain measurement method". *Strain,* ***46***(3), pp. 258–266.

[10] Iliopoulos, A. P., Michopoulos, J. G., and Andrianopoulos, N. P., 2008. "Performance sensitivity analysis of the Mesh-Free Random Grid method for whole field strain measurements". *ASME Conference Proceedings,* ***2008***(43277), pp. 545–555.

[11] Iliopoulos, A. P., and Michopoulos, J. G., 2009. "Effects of anisotropy on the performance sensitivity of the Mesh-Free random grid method for whole field strain measurement". *ASME Conference Proceedings,* ***2009***(48999), Jan., pp. 65–74.

[12] Michopoulos, J. G., and Iliopoulos, A. P., 2009. "A computational workbench for remote full field 2d displacement and strain measurements". *ASME Conference Proceedings,* ***2009***(48999), pp. 55–63.

[13] Iliopoulos, A. P., Michopoulos, J. G., and Andrianopoulos, N. P., 2010. "Performance analysis of the Mesh-Free Random Grid Method for full-field synthetic strain measurements". *Strain*, p. In Print.

[14] Michopoulos, J., and Iliopoulos, A., 2011. "A computational workbench for remote full field 3d displacement and strain measurements". In Proceedings of the ASME 2011 International Design Engineering Technical Conferences & Computers and Information in Engineering Conference IDETC/CIE, August 29-31, 2011, Washington, DC, USA.

[15] Iliopoulos, A., Michopoulos, J., Orifici, A. C., and Thomson, R. S., 2011. "Experimental validation of the 2d meshless random grid method". In Proceedings of the ASME 2011 International Design Engineering Technical Conferences & Computers and Information in Engineering Conference IDETC/CIE, August 29-31, 2011, Washington, DC, USA. Submitted.

[16] Iliopoulos, A., and Michopoulos, J., 2013. "Direct strain tensor approximation for full field strain measurement methods". *International Journal of Numerical Methods in Engineering*. In Print.

[17] Iliopoulos, A., and Michopoulos, J., 2012. "Direct strain imaging for full field measurements". In ASME 2012 International Design Engineering Technical Conferences & Computers and Information in Engineering Conference IDETC/CIE, August 13-15, 2012, Chicago, IL, USA.

[18] Cheng, P., Sutton, M., Schreier, H., and McNeill, S., 2002. "Full-field speckle pattern image correlation with b-spline deformation function". *Experimental Mechanics,* ***42***, pp. 344–352. 10.1007/BF02410992.

[19] Michopoulos, J. G., Hermanson, J. C., and Iliopoulos, A., 2010. "Towards a recursive hexapod for the multidimensional mechanical testing of composites". *ASME Conference Proceedings,* ***2010***(44113), pp. 91–99.

[20] Michopoulos, J., C., H. J., and Iliopoulos, A., 2012. "Robotic and multiaxial testing for the constitutive characterization of composites". In Materials Challenges in Alternative & Renewable Energy, February 26-March 1, 2012, Clearwater, FL, USA.

[21] Michopoulos, J., Hermanson, J. C., and Iliopoulos, A., 2012. "First industrial strength multi-axial robotic testing campaign for composite material characterization". In Proceedings of the ASME 2012 International Design Engineering Technical Conferences & Computers and Information in Engineering Conference IDETC/CIE, August 12-15, 2012, Chicago, IL, USA.

[22] Hartley, R., and Zisserman, A., 2004. *Multiple View Geometry in Computer Vision*, 2 ed. Cambridge University Press, Apr.

[23] Mase, G., 1969. *Schaum's Outline of Continuum Mechanics*, 1 ed. McGraw-Hill, June.

[24] Belytschko, T., Krongauz, Y., Organ, D., and Fleming, M., 1996. "Meshless methods: An overview and recent developments". *Computer Methods In Applied Mechanics And Engineering,* ***139***, pp. 3—47.

[25] Lu, Y. Y., Belytschko, T., and Gu, L., 1994. "A new implementation of the element free galerkin method". *Computer Methods in Applied Mechanics and Engineering,* ***113***(3-4), pp. 397–414. cited By (since 1996) 379.

[26] Liu, G. R., 2002. *Mesh Free Methods: Moving Beyond the Finite Element Method*, 1 ed. CRC Press, July.

[27] Lekhnitskii, S. G., 1981. *Theory of Elasticity of an Anisotropic Elastic Body*. Mir Publishers, Moscow.

[28] Savin, G. N., 1961. *Stress Concentration around holes*. Pergamon Press, London.

[29] Chern, S., and Tuttle, M., 2007. "On displacement fields in orthotropic laminates containing an elliptical hole". *Journal of Applied Mechanics,* ***67***, September, pp. 527–539.

[30] The Mathworks. Matlab. http://www.mathworks.com.

[31] Iliopoulos, A., Michopoulos, J. G., and Hermanson, J. C., 2012. "Composite material testing data reduction to adjust for the systematic 6-DoF testing machines aberrations". In 2012 ASME International Design Engineering Technical Conferences & Computers and Information in Engineering Conference,Chicago IL, USA.

This material is declared a work of the U.S. Government and is not subject to copyright protection in the United States.
Approved for public release; distribution is unlimited.